Journal of Studies in Science and Engineering

EngiScience Publisher

Research Article

Combining Thermal and Optical Modeling to Optimize the Performance of a Flat Plate Absorber at Various Locations in a Solar Air Collector

Hiwa Abdlla Maarof [1,*], Mohammad Shamsi [2]

[1] Department of Physics, College of Science, University of Halabja, Halabja, 46018, Iraq

[2] Process Engineering Department, Faculty of Chemical Engineering, Tarbiat Modares University, Tehran, 14115, Iran

*Corresponding Author: Hiwa Abdullah Maarof, E-mail: hiwa.maarof@uoh.edu.iq

Article Info

Article History

Received Aug 14, 2022

Revised Aug 27 , 2022

Accepted Aug 30, 2022

Keywords

Solar Air Heater

3-D CFD Modeling

Optical and Thermal Modeling

Heat Transfer Coefficient

Nusselt Number

Thermal Efficiency

Abstract

Increasing the absorber plate surface in a solar air heater system (SAHs) can increase thermal efficiency, heat transfer coefficient, and Nusselt number. This paper includes the development of a 3-dimensional computational fluid dynamics (3-D CFD) model for predicting the location of the absorber plate from the bottom of the collector, followed by its validation using experimental data. Various geometrical types are investigated to determine optimal design features, such as Type I, Type II, Type III, Type IV, and Type V. A comprehensive analysis is performed to achieve this goal, including thermal efficiency, heat transfer coefficient, and Nusselt number analyses. Results indicate that Type V has better performance than other geometries. When the absorber plate location Type V with a distance (dis) of 0.012 m far from the bottom of the collector. As a result, increases in the average thermal efficiency, heat transfer coefficient, and Nusselt number of the system are 19 %, 53%, and 268.8%. Compared to Type I, when the absorber plate was lying on the collectors without a gap between the absorber and collector bottom.

1. Introduction

1.1. Solar Energy and the Demand for Clean Energy Resources

Global economic progress and industrialization have become increasingly dependent on various forms of energy, including solar energy, an essential energy source in light of climate change and sustainable development. Light and heat are both forms of solar energy. A significant advantage of this renewable energy is that it is one of the most significant and promising energy sources. It is estimated that the sun's energy that falls on the surface of the Earth is about ten thousand times our current energy requirements [1].

In recent years, there has been an essential change in the adaptation of solar energy because of the global efforts to improve access to and ensure energy security and mitigate climate change [2–4]. As solar

radiations produce a large amount of energy, making it a valuable and limitless resource that can be collected by Solar Air Heaters (SAH), Solar Water Heaters (SWH) and Photo Voltaic (PV) collectors. SAHs are the most basic method of converting solar energy into thermal energy and are one of the most popular types of solar thermal systems due to their ease of use and low cost [5].

Solar radiation, both direct and diffuse, is absorbed in the absorber plate, which transfers this energy to the air flowing through the absorber plate. The beneficial heat gain by the collector fluid determines the thermal efficiency of solar air heaters [6]. There are a variety of applications for SAHs, including solar drying [7–10], solar thermal power [11–13], concentrated solar power [14,15], solar ponds [16,17], solar space heating and cooling [18–20], solar furnaces [21], and solar water heating [18,22]. Many researchers have tested the effectiveness of the SAH systems through the use of various geometries. In addition, baffles, slotted absorbers, and filled absorbers are among these improvements. In all of these methods, heat is transferred from the absorber plate to the air [23–28].

1.2. Solar Air Heaters, Literature Review

The use of various types of SAHs has been reported in several studies. Kumar et al. [29] experimentally investigated the thermal energy and outlet temperatures of a channel with winglet-shaped ribs roughened surface. The experimental results showed an increased thermal efficiency from 17 % to 46 % compared to the smooth channel.

Aboghrara et al. [30] tested corrugated absorber jet impingement through circular jets in a duct flow of solar air heaters plates and compared them with flat plate absorbers. They found that the inflow jet impingement on corrugated plating absorbers has a substantial heat transfer enhancement effect. It is observed that the proposed design duct has almost 14% higher thermal efficiency compared with the smooth duct. Luan et al. [31] experimentally analyzed inclined baffles with angles from 60° to 120° that caused the most significant turbulence due to increasing degree of blockage and obtained higher efficiencies.

Singh et al. [32] experimentally evaluated flat plate and flat plate with small cylindrical tubes with and without phase change material (PCM), reporting about 2°C to 9°C higher temperature difference between ambient air and exhaust air compared to SAH with a flat plate absorber on forced convection and also supplied outlet temperatures at about 48 ◦C for approximately 9.8 hours/day and with 66% daily efficiency. Azad et al. [33] Performed a comprehensive experimental and numerical comparison between the

rib elements diameter (g/e) of 2, 3, 4, and 5 at an airflow angle 30◦, at Reynolds numbers 3000 to 14000 and demonstrated that Nusselt number is maximally enhanced at g/e equal to 4, which is 3.88 times greater than smooth plates.

Saravanan et al. [34] conducted an experimental investigation of the SAHs utilizing multiple staggered C-shaped finned absorbers, both perforated and unperforated, with a 3.3 to 3.8 ratio of pitch to the gap, 0.3 to 0.7 ratio of height, and 1.5 to 3 ratio of perforations, to maximize heat transfer. The highest thermal performance was achieved at the relative pitch to gap ratio of 3.8, the relative height ratio of 0.6, and the corresponding perforation ratio of 3. For 3.8 and 0.6 relative pitch to gap ratios and 0.6 relative height ratios, respectively, thermal performance and friction factor of C-shaped finned absorber plates without perforated holes were 2.61 and 5.93 times higher than flat absorber plates. Khanlari et al. [35] performed experimental and numerical analysis on a tube-type SAH drying process, and the results indicate that it can achieve an efficiency of 45.6-56.8%.

Abo-Elfadl et al. [36] compared single-pass flat plate SAH and single-pass tubular SAH at 0.025 kg/s and found increased thermal and exergy efficiencies in single-pass tubular SAH compared to single-pass flat plate SAH with attained thermal and exergy efficiencies of 133% and 330%, respectively. Singh et al. [37] experimentally and numerically surveyed the thermal performance of a porous serpentine wavy wire mesh packed bed solar air heater. Investigations showed that in a 93% porous double pass serpentine packed bed SAH, the thermal and thermohydraulic efficiencies were approximately 80% and 74%, respectively 18% and 17% higher than a single pass.

Bensaci et al. [38] conducted numerical and experimental studies on the baffle placement with Reynolds numbers from 2370 to 8340. They analyzed the effects of baffle positions on convective heat transfer coefficients. The results showed that SAHs achieve the best thermo-hydraulic efficiency when the baffles are located in the first 50% of the air channel. Yadav et al. [39] proposed the maximum improvement in heat transfer of SAHs, used a roughness absorber surface, and developed the Nusselt number and friction factor. The results obtained were 2.89 and 2.93 times compared with a smooth absorber surface. Saini et al. [40] experimentally studied the heat transfer coefficient of SAHs and used arc-shape parallel wire on the absorber surface, predicting parameter effects. One was the Nusselt number. Results show that an increased Nusselt number affected to increased heat transfer coefficient. Farhan et al. [41] conducted an experimental

and numerical study of the energy and exergy efficiency of v-corrugated SAHs where twisted tape inserts were placed within the air passages formed by the absorber and backplate. The results revealed that thermal and thermohydraulic efficiencies, when compared to absorbers without twisted tape, can be increased by 17.5 and 17%, respectively.

Esen et al. [42]. proposed a Wavelet Neural Network (WNN), a neural network (ANN) modeling of SAHs, and an optimization method based on WANs. Based on predictions and experimental results for variations in airflow rates and ambient conditions of an absorbing surface SAH, the proposed WNN model allowed them to estimate the efficiency of SAHs more accurately.

1.3. Research Gap, Challenges, and Novelties

An analysis of solar heaters' shortcomings in the presence of an air absorber plate is presented here, and a proper strategy is proposed to improve SAH's efficiencies. A 3D CFD model of a flat plate in SAHs based on the experimental results. This model uses the Optics Geometric component in combination with the heat transfer in solid and fluid components to evaluate the daily performance of different absorbing surfaces and absorber plate locations using the instantaneous actual flux distributions. The radiative and heat losses are taken into account.

Validation of the model is based on experimental evidence produced from a system with the same components and dimensions under various operating conditions. After simulation validation, the model was modified for various absorber plate locations, and the system thermal efficiency analysis was carried out. Finally, the efficiency of the air heater from the viewpoints of outlet temperatures, thermal efficiency, heat transfer coefficient, and Nusselt number was evaluated. The simulation was done using COMSOL Multiphysics 5.6, which is versatile and can perform the simulation of multi-physics problems very well.

2. Experimental Conditions

A clean daytime environment was used for testing Esen [42]. Firat University, Faculty of Technical Education, Turkey, installed and measured a SAH in Elazig (latitude 38.41 N, altitude 1067 m above sea level, longitude 39.14 E). SAHs can be modeled using a WNN-based optimization method. Based on predictions and experimental results, estimate the efficiency of SAHs more accurately with the proposed WNN model. SAHs with an absorbing surface and their airflow rates. A schematic and a diagram of the flat plate absorber are shown in Figure 1. The absorber plate was used in this application. The stainless-steel absorber

was coated with black chrome. This absorber has a dimension of 0.84, 2.14 m, and a thickness of 1 mm. The glass was 5 mm thick. The collector used a single cover glass. After installation, the collector ran for many days under normal weather conditions. Evenly spaced thermocouples on the absorber plate measured the collector's inlet and outlet temperatures using two thermocouples with well-insulated leads.

The environment temperature was measured with a mercury thermometer behind the collector. To determine whether Collectors are exposed to a total amount of solar radiation, a Kipp and Zonen CM 11 Pyranometer was used. The meter is adjacent to the glazing cover and on the same plane. Solar radiation was measured automatically by a Kipp and Zonen CC 12 solar integrator. An airflow meter (Lutron AM-4206M digital anemometer) was used to collect data at 30-minute intervals on insolation, working fluid outlet and inlet temperatures, ambient temperature, and absorbing plate temperature. Radial fans provided the air with a maximum power of 0.537 kW each. The collector's outlet was fitted with an air-sucking radial fan. Inlet and outlet pressure losses were measured with a digital manometer (AZ 82100).

a b

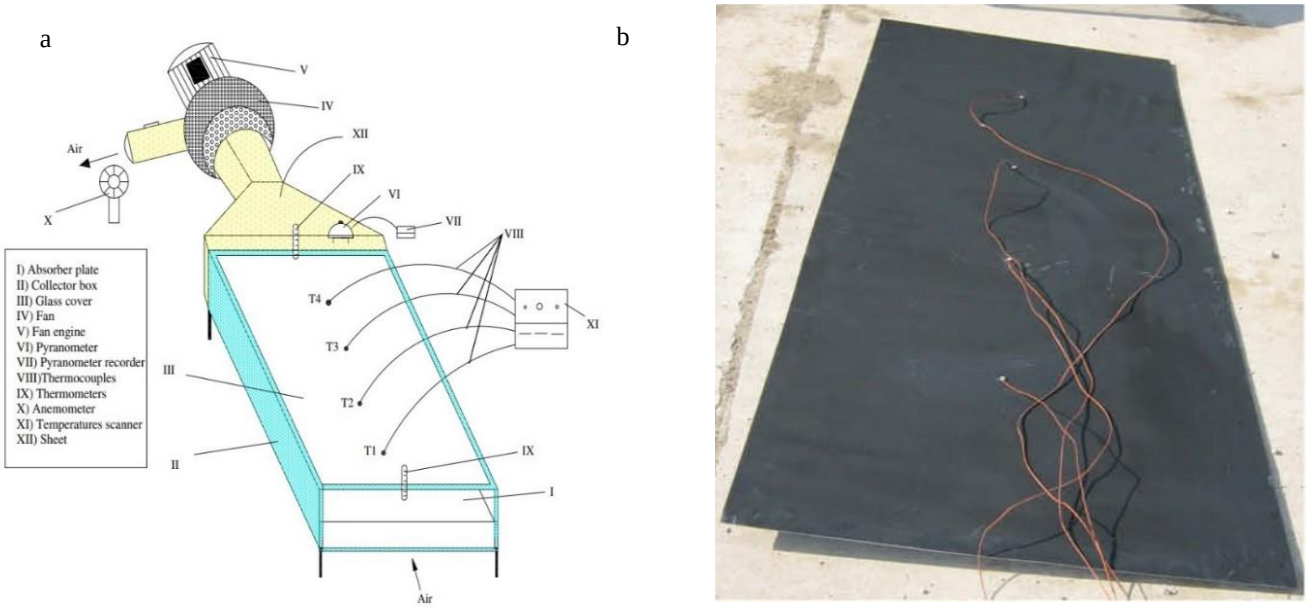

Figure 1. a) Diagram of the SAHs, b) flat plate absorber of the experimental

This study simultaneously measured the ambient temperature, collector temperatures, air velocity, pressure, and solar radiation as the air passed through the duct and moved through the collectors. A digital manometer (AZ 82100) has a 3% accuracy, and a Kipp and Zonen CM11 Pyranometer has a 1% accuracy. At the same time, the experiment was conducted using T-type thermocouples, which are accurate to 0.018

degrees Celsius, metal-vane anemometers (AM-4206M, air velocity + airflow), and Kipp and Zonen CM11 Pyranometers. A series of tests were administered between 9:00 to 16:00.

3. Explanation Analytical

3.1. Optical Modeling

The Geometric Optics (GOP) module of the COMSOL Multiphysics software 5.6 is used to simulate ray trajectory in the SAHs and gather realistic solar flux distributions on the absorber's surface and position from the base of the collector. This model calculates distributed fluxes and solar thermal energy absorbed by surfaces based on the optical properties of the glass cover and absorb plate. This ray tracing model reflects the original optical properties of all components. Glass is modeled to have a transmission coefficient of 0.9, an emissivity of 0.5, and an absorption coefficient of 0.9 for the absorbing coating. The components of the design are shown in Figure 2.

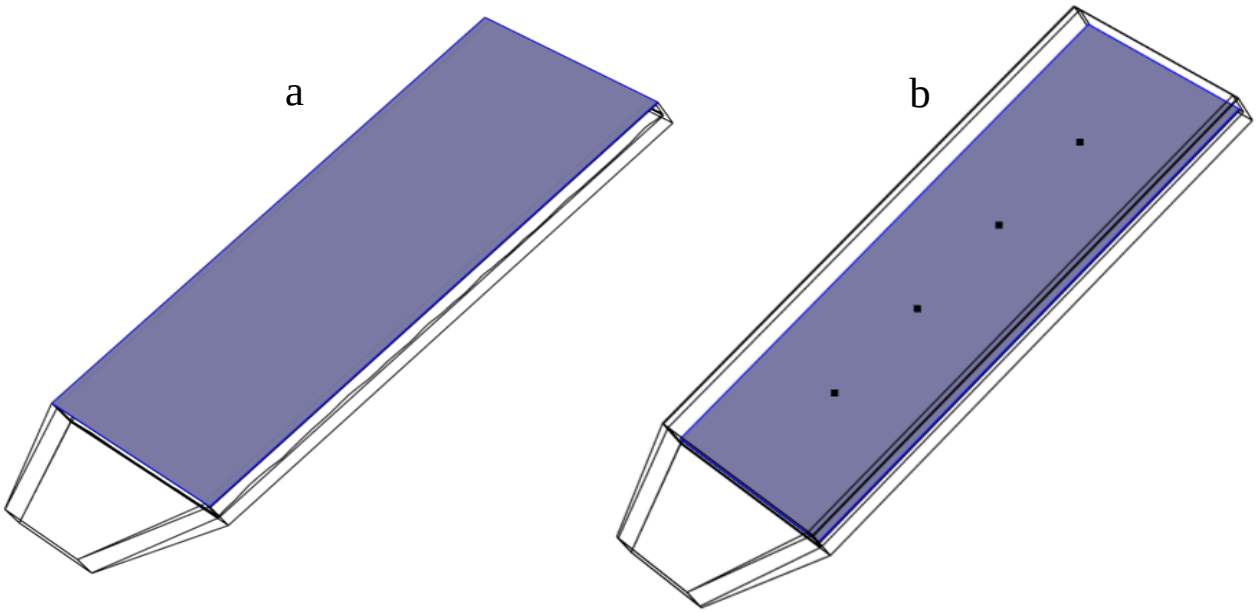

Figure 2. an optical system consists of (a) glass cover, (b) absorber plate

In Wavefront Ray Tracing, the ray directions and incidence angles are determined using the Fresnel equation and Snell's law. Each ray's propagation can be described by first-order equations coupled together.

$$\frac{dq}{dt} = \frac{\partial w}{\partial k} \tag{1}$$

q represents the position vector

$$\frac{dk}{dt} = -\frac{\partial w}{\partial q} \tag{2}$$

k represents the wave vector

$$\theta_i = a\cos\left(\frac{n_i.n_s}{|n_i||n_s|}\right) \tag{3}$$

(*ni*) is a normal vector in the domain of air that (θi) and (*ns*) represent the normal angle of incidence and a unit vector for incident rays. Reflected rays travel in the same direction as (*nr*):

$$n_r = n_i - 2n_s\cos\theta_i \tag{4}$$

n_t represents the propagation direction of the refracted ray. The following expression relates angular frequency and ray vector:

$$w = \frac{c}{n} \tag{5}$$

The model shows that the glass cover is transparent, allowing solar radiation to pass through it. A very slight diffuse and specular reflection is visible from the surface, as shown in Figure 2.a. Next is the black absorber plate, which is more thermally conducting, as shown in Figure 2.b.

3.2. Optical-thermal model combined

To understand the related phenomena within a system, it is critical to examine the impacts of the essential parameters on its performance. Developing an accurate and helpful model requires being comprehensive, straightforward, and able to describe and predict behavior under conditions similar to the real world. An optical system model is proposed, and then a thermal and fluid flow model is constructed using the heat flux distribution from the optical model. To determine whether solar flux distributions on absorbing plates are not uniform, we used the geometric optics module in COMSOL Multiphysics.

3.3. Modeling of Energy and Fluid Flow

As ambient and time variations in solar radiation affect incoming solar radiation, it is evaluated as the system is operated to estimate its energy balance under unsteady-state conditions. As a result of energy balance across the entire system, the following equation can be expressed:

$$\frac{\partial\left(\rho C_p T\right)}{\partial t} + \rho C_p u.\nabla T + \nabla.\left(-k\nabla T\right) = 0 \tag{6}$$

Thermal capacity is expressed by C_p density ρ, and thermal conductivity by *k* in this formula. Additionally, *u* represents the airflow velocity field through the box.

Table 1. Thermal and Optic Geometric Properties of Solar Air Heaters.

Parameters and components	**Specifications, properties, and values**
Sun rays' number	100,000
Index of refraction of exterior domains	1
Maximum secondary ray number	0
SAH(Glass)	Solar transmittance of glass: 0.9 Glass solar absorption: 0.02 The refraction index of glass: 1.45 The emissivity of the glass: 0.5
Irradiance and power	maximum irradiance: 970 W/m^2 Average irradiance: 809 W/m^2 Max. power: 1797 W.
SAH	Solar air collector thickness: 0.03 m Solar air collector length: 2.14 m Solar air collector width: 0.84 m Collector angle: (30 °).
Glass	Glass thickness: 0.005 m Glass density: 2203 kg/m^3
SAH (absorber)	Heat transfer fluid: Air Absorber material: copper Collector area: 1.8 m^2 Absorber thickness: 0.001 m Coating emissivity: 0.94 Absorber thermal conductivity: 400 W/(m.K)
Operational Parameters	Inlet mass flowrate: 0.02-0.06 kg/s. Inlet temperature: 24-38.6 °C Wind velocity: 1 m/s Ambient temperature: 24-38.6 °C

In the Geometric Optics module, thermal analysis was applied to determine how much heat should be absorbed on the collector walls by a solar heat plate. In order to calculate the energy formula, embedded solar heat must be taken into account. The heat flux of a system also includes thermal loss analysis. Using Newton's cooling law, convective heat is calculated by measuring the amount of heat transferred from the surface of the glass to the surrounding air.

$$Q_{loss,conv} = h_{conv} A_{glass} \left[T_{glass}(t) - T_{amb}(t) \right] \tag{7}$$

An air surface and a glass surface are coupled by convection induced by h_{conv}. A flat plate absorber's radiative heat loss is based on using the Stefan-Boltzmann radiation exchanging equation:

$$Q_{loss,rad}(t) = \varepsilon \sigma A_{abs} \left[T_{s,abs}^4(t) - T_{amb}^4(t) \right] \tag{8}$$

The ε parameter measures how much light the absorber absorbs and provides this Stefan-Boltzmann constant. Collectors have thermally insulated sides and bottoms.

In this study, the inlet air mass flow rate ranges between 0.02 and 0.08 kg/s. Thus, the Reynolds number of the air should be used to select the fluid flow model module. The purpose is to determine the velocity field inside the SAHs. The equation is as follows:

$$\frac{\partial \rho}{\partial t} + \nabla.(\rho u) = 0 \tag{9}$$

The momentum formula describes how air moves in the collector:

$$\rho \frac{\partial u}{\partial t} + \rho (u.\nabla) u = \nabla.\left[-pI + (\mu + \mu_T)(\nabla u + (\nabla u)^T) \right] + \rho g \tag{10}$$

Time-dependent governing equations determine the thermal efficiency of the SAHs.

$$\eta_{th}(t) = \frac{\dot{m} c_p \left[T_{Out}(t) - T_{In}(t) \right]}{I_g(t) A_c} \tag{11}$$

Nu is determined as follows:

$$Nu = \frac{h \times D_h}{K} \tag{12}$$

h the heat transfer coefficient in the SAHs determined as follows:

$$h = 2.8 + 3U_{wind} \tag{13}$$

D_h is a hydraulic diameter calculated as follows:

$$D_h = \frac{A_{cross}}{P_{wet}} \times \frac{L_c}{L_c} = \frac{4V_{air}}{A_{contact}} \tag{14}$$

3.4. Defining the boundary and the initial conditions

These boundary conditions govern collector air flow rates and heat transfer:

$$-\int \rho (u.n) ds \,|_{in} = \dot{m} \tag{15}$$

$$T_{in}(t) = T_{amb}(t) \tag{16}$$

A heat absorber plate displays the amount of heat absorbed as follows:

$$-n.k\nabla T\,|_{boundary} = Q_b \tag{17}$$

When solving time-dependent governing equations, the absolute ambient temperature at the time the system was started is assumed.

$$T_{In} = T_{amb} \tag{18}$$

4. Model Validation and Mesh Independence Analysis

4.1. Grid validation independently

The mesh elements in the CFD modeling were created using a free tetrahedral grid in COMSOL Multiphysics. When a mesh control custom mesh generation defines this parameter, highly dense meshes are generated for the absorber plate, solar air heater, and air within the collector. Provides qualitative insight into how the mesh was shaped for modeling the system shown in Figure 3. A margin of error below 3% estimates the input solar energy due to developing independence criteria for meshes. Air running through the collector absorbs the sum of heat. Table 2. provides information on the number of grids. With the increase in the number of cells, outlet temperatures remained unchanged due to the mesh study. It is evident from Table 2. that a total of 803819 cells were independent.

4.2. Model verification

As part of this validation, experimental results were compared to the model's predictions to ensure that the proposed model is accurate. Various operating conditions are compared in Table 3. The average air temperature in the system is estimated by comparing models with experimental data (T1, T2, T3, T4, and T_{outlet}). In order to validate a model, (T1, T2, T3, T4, and T_{outlet}) must be measured relative to each other. Eqs can be used to express these errors.

$$E_T = \left| \frac{T_{Out,num} - T_{Out,Exp}}{T_{Out,Exp}} \right| \times 100 \tag{19}$$

Despite various operating conditions, model results and experimental data show good agreement in Table 3. It is also parametrically suitable, in addition to being reliable. Therefore, the system's heat losses can be considered when evaluating the model.

Table 2. Mesh Independence Analysis

Time(h)	Mesh Elements Specifications			Exp. Temperature(°C)	Model Temperature (°C)	Relative Error (%)
	Domain	Boundary	Edge			
11:00	384675	77234	2404	42.5	43.4	3.56
	691952	148524	3534	42.5	43.1	3.67
	803819	172871	3767	42.5	42.9	3.7
	844703	179059	4127	42.5	43.12	3.65
13:00	384675	77234	2404	41	43.75	2.83
	691952	148524	3534	41	43.23	2.99
	803819	172871	3767	41	42.89	3
	844703	179059	4127	41	43.53	2.9
14:00	384675	77234	2404	38	40.57	1.85
	691952	148524	3534	38	40.12	1.99
	803819	172871	3767	38	39.93	2
	844703	179059	4127	38	40.31	1.93
15:00	384675	77234	2404	32	36	0.44
	691952	148524	3534	32	35.62	0.57
	803819	172871	3767	32	35.44	0.63
	844703	179059	4127	32	35.73	0.54

4.3. Solar Fluxes and Ray Trajectory Distributions

Solar air collectors are predicted to have ray trajectories and flux distributions. The collector surface interferes with reflections on the absorbing surface and concentrates them in irregular patterns. To show how rays cross a collector, a ray is focused on an absorbing surface shown in Figure 5. a., A surface with a distributed solar flux. A collector surface's solar flux distribution is also shown in Figure 5. b.

Table 3. Model Validation with Experimental Results

Ta_in (^{0}C)	Model.T1 (^{0}C)	Exp.T1 (^{0}C)	R_Error (%)	Model.T2 (^{0}C)	Exp.T2 (^{0}C)	R_Error (%)	Model.T3 (^{0}C)	Exp.T3 (^{0}C)	R_Error (%)
23.1	25.0	25.3	1.0	25.00	26.2	4.0	27.00	27.1	0.4
27.1	34.2	35.4	3.9	37.13	38.2	2.8	39.28	39.8	1.7
31.2	39.4	39.5	0.4	43.03	44.0	2.2	46.41	46.5	0.3
33.8	42.8	42.5	1.0	45.93	47.2	4.0	51.07	53.0	5.9
35	44.4	45.9	4.7	47.74	49.5	5.5	53.21	56.6	0.3
36.6	41.7	41.0	2.3	44.95	45.0	0.1	50.25	49.9	1.1
37.9	37.9	38.0	0.2	40.73	42.0	4.0	45.33	44.0	4.2
39.2	33.2	32.0	3.9	35.40	34.8	1.9	37.04	36.0	2.9
39.9	25.0	25.3	1.0	25.00	26.2	4.0	26.00	27.1	4.0
38.6	34.2	35.4	3.9	37.13	38.2	2.8	39.28	39.8	1.7
37	39.4	39.5	0.4	43.03	44.0	2.2	46.41	46.5	0.3
35.6	42.8	42.5	1.0	45.93	47.2	4.0	51.07	53.0	5.9
34	44.4	45.9	4.7	47.74	49.5	5.5	53.21	56.6	0.3
33.4	41.7	41.0	2.3	44.95	45.0	0.1	50.25	49.9	1.1
29.8	37.95	38.0	0.2	40.73	42.0	4.0	45.33	44.0	4.2
Average Relative Error %			**2.0**			**3.1**			**2.3**

Ta_in (^{0}C)	Model.T4 (^{0}C)	Exp.T4 (^{0}C)	R_Error (%)	Model.T_out (^{0}C)	Exp.T_out (^{0}C)	R_Error (%)
23.1	27.00	27.7	2.5	29.10	29.0	0.34
27.1	41.19	41.1	0.3	43.18	41.9	4.1
31.2	49.12	48.0	3.5	50.30	49.9	0.8
33.8	54.30	55.1	2.4	58.20	56.9	3.9
35	57.67	59.2	2.6	60.97	62.9	5.7
36.6	53.62	53.0	1.9	58.01	56.8	3.7
37.9	48.28	46.5	5.6	52.29	49.0	0.2
39.2	39.40	37.4	5.3	44.71	39.0	8.3
39.9	26.50	27.7	4.3	25.00	29.0	3.2
38.6	41.19	41.1	0.3	43.18	41.9	4.1
37	49.12	48.0	3.5	50.30	49.9	0.8
35.6	54.30	55.1	2.4	58.20	56.9	3.9
34	57.67	59.2	2.6	60.97	62.9	5.7
33.4	53.62	53.0	1.9	58.01	56.8	3.7
29.8	48.28	46.5	5.6	51.29	49.0	4.67
Average Relative Error %			**3.0**			**3.5**

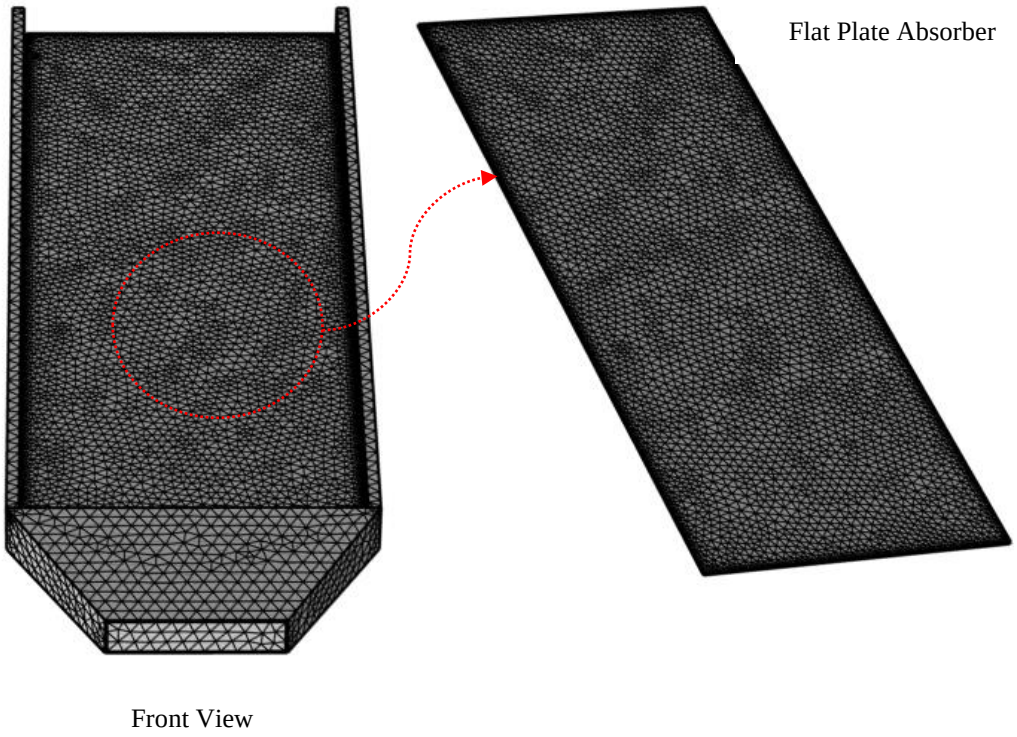

Figure 3. The meshes generated for the CFD simulation of solar collectors

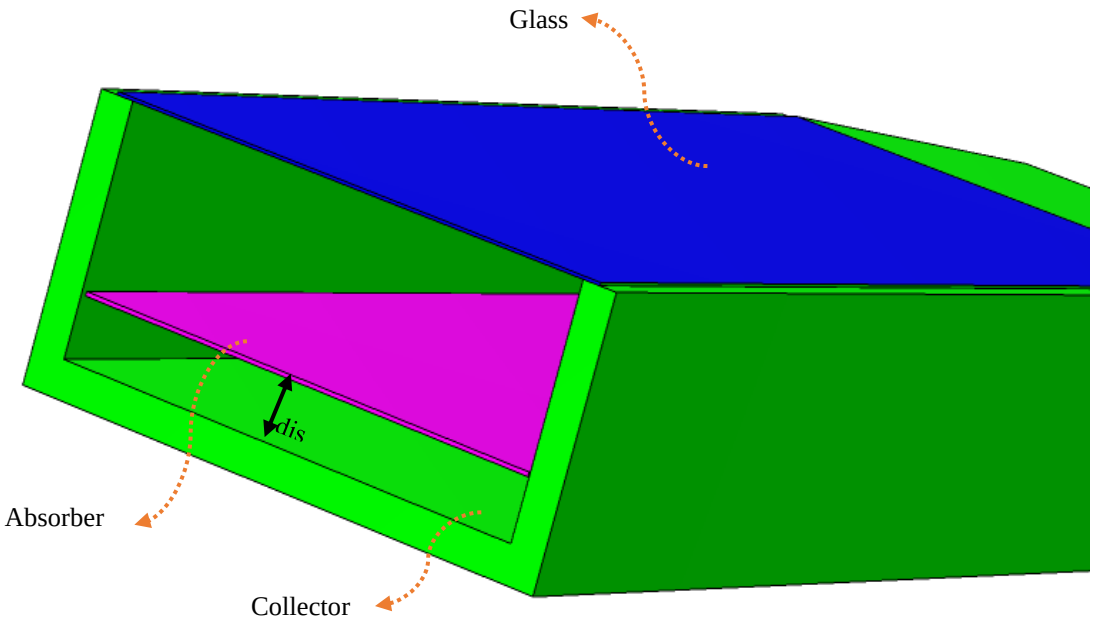

Figure 4. The location of the absorber plate relative to the collector bottom line.

Type I=0 mm, Type II= 3mm, Type III= 6mm, Type IV= 9 mm, and Type V=12mm

4.4. Analyzing Thermal Data

Several distances between the absorber and base of the collector in the same conditions are chosen for the model simulation to compare the outcomes of the SAHs with various absorb position distances. In

particular, the normalized ambient temperature and solar irradiation values for a typical workday in Jul in Yasouj (a city in southwest Iran with latitudes of 30.6684 N and 51.5875 E, respectively, are chosen for this purpose. Irradiation from the sun and ambient temperature are shown in **Figure 6**. In the simulations, inlet mass flow rates and ambient wind velocity are taken as 0.02 m/s and 0.08 kg/s, respectively.

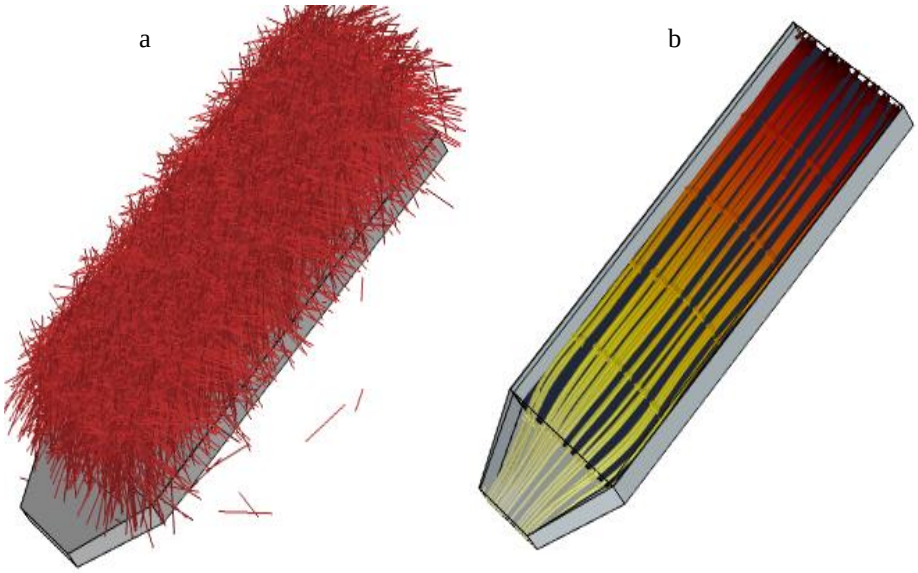

Figure 5. An example of the ray paths and heat flux on the solar air heater

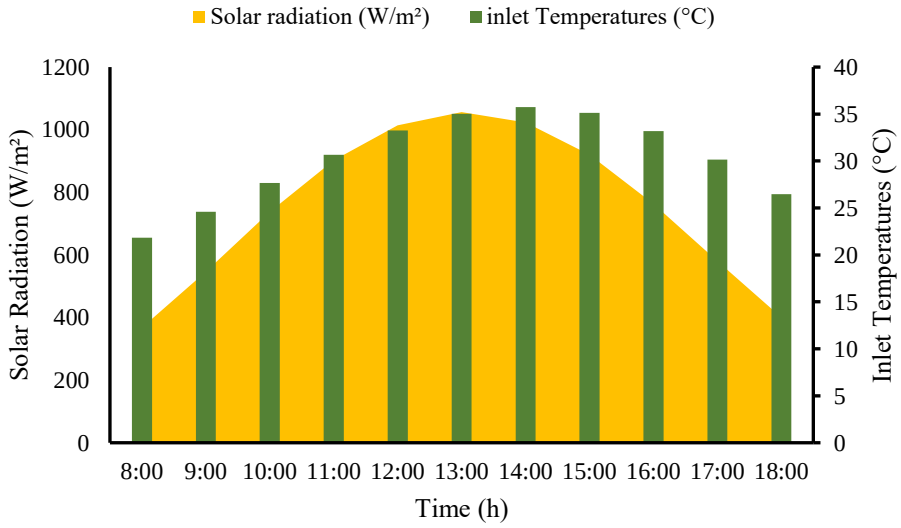

Figure 6. On a typical day in July, in Yasouj, Iran, ambient air temperature and solar irradiation [43].

5. The Results and Discussion

The use of plate Type V is the measure to enhance the heat transfer by providing more heat transfer area to air in the same length of the absorber plate compared to plate Type I, Type II, Type III, and Type

IV. when the user Type V more heat is received because the amount of air that flow over the absorber also flows under the absorber, which provides more heat, and reduce heat losses. The temperature of the outlet air of the system for different locations of the absorber plates at a 0.02 kg/s mass flow rate is shown in Figure 7. A range of maximum temperatures was measured for Tout Type I, Tout Type II, Tout Type III, Tout Type IV, and Tout Type V, which are 75.37, 73.98, 77.87, 82,9, and 83 °C, respectively. During the late afternoon, solar radiation increases, and the heaters' temperatures increase to their maximum value at 14:00. Consequently, the plate surface heaters Type V has higher outlet temperatures than other Types of flat plate heaters. Computational fluid dynamics (CFD) and heat transfer tools have been used to investigate solar air heaters, revealing their physics and rendering them powerful tools for optimizing flow and geometrical parameters.

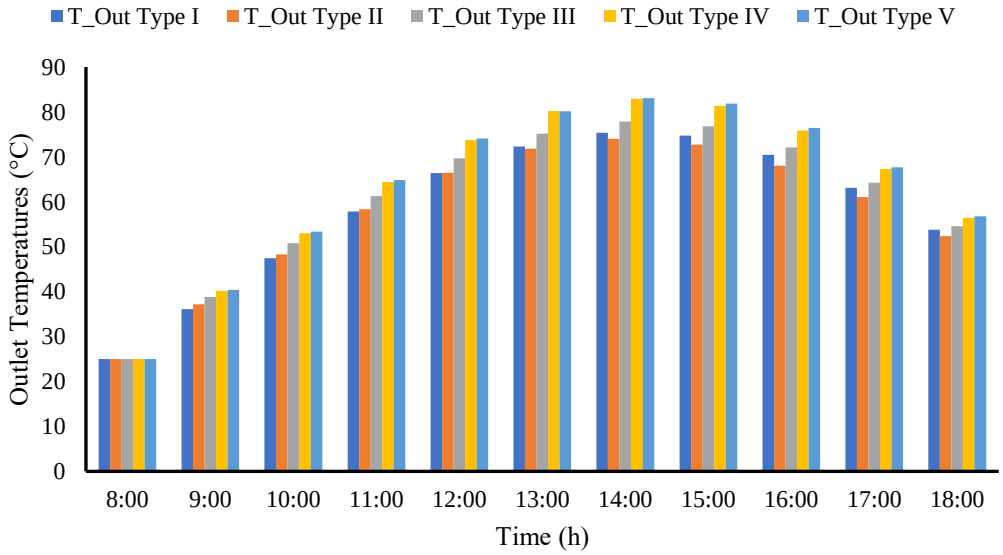

Figure 7. The temperature of the air outlet at different distances a flat absorber from the collector base.

Temperature efficiency with various absorber locations from the bottom of the collector. There is a decrease in values during the middle of the day compared to the morning and evening. Due to the higher temperature of the system's primary components at midday, there are more thermal losses at that time. Also, the thermal efficiencies of the systems are higher at the end of the day than at the beginning of the day. Earlier conditions impact the system's immediate performance while it operates under changing operational settings. In such solar systems, a portion of the absorbed solar heating capacity is absorbed in different faces of the system as sensible heat. This is done as air passes through the SAHs and is in heat contact with adjacent components. When the solar irradiation decreases, the absorber absorbs less heat, decreasing air

temperature. This results in sensible heat being transferred in the opposite direction from the collector's components to the air, leading to higher thermal efficiency, based on Figure 8. SAH, the absorber location at the bottom of the collector, is 1.2 cm and has the highest average daily thermal efficiency. The system's thermal efficiency is significantly affected by the different locations of the absorber plates. At a mass flow of 0.02 kg/s, Type I, Type II, Type III, Type IV, and Type V of SAH are compared for their instantaneous thermal efficiency. Solar radiation is measured at 368-1056.4 W/m2, and the maximum values are 76.5, 72.35, 78.3, 83.77, and 84.75%, respectively. With the location of the absorber plate, the surface area can be increased, leading to faster convection heat transfer. The air heater becomes more efficient as a result. Also, compared with the case without distance, heater efficiency increases by 8.2% when choosing a suitable location for absorber plates.

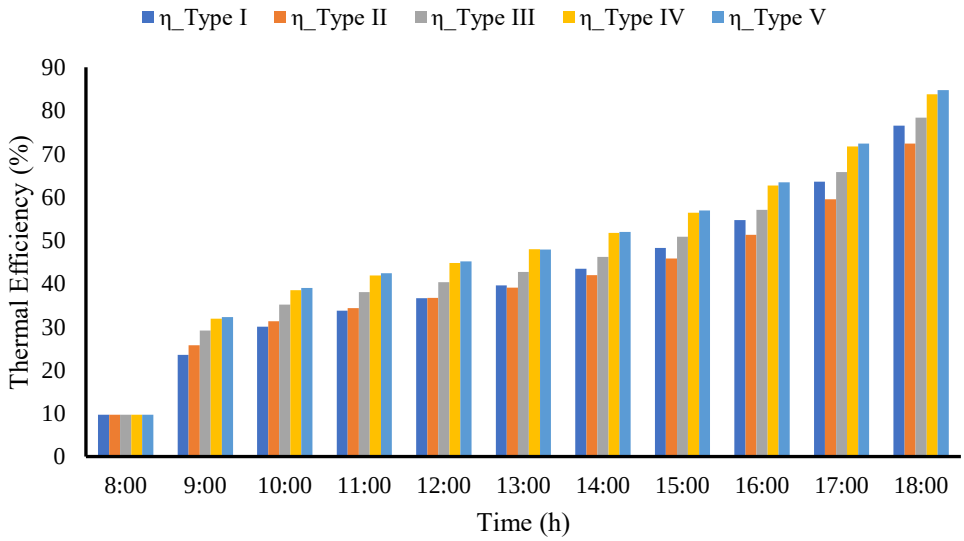

Figure 8. The variation in thermal efficiency

Heat flows through the insulation of the collector mainly by conduction, which is the reason for energy loss through the bottom and edges. Absorbers' plate location affects local convective heat transfer coefficients when the airflow through the top and bottom absorbers' surfaces is shown in Figure 9. Heat transfer coefficients are higher with increased surface area. Compared with mornings and evenings, the values decrease during the middle of the day. At midday, there are more heat losses because the system's primary components are at a higher temperature. The heat transfer coefficient is higher than at the beginning. The instantaneous heat transfer coefficient of Type I, Type II, Type III, Type IV, and Type V of SAH is

compared at a mass flow rate of 0.02 kg/s. According to the measurements, solar radiation ranges from 368 to 1056.4 W/m^2, with maximum values of 9.67, 7.7, 9.41, 14.56, and 17 (W/m^2. K).

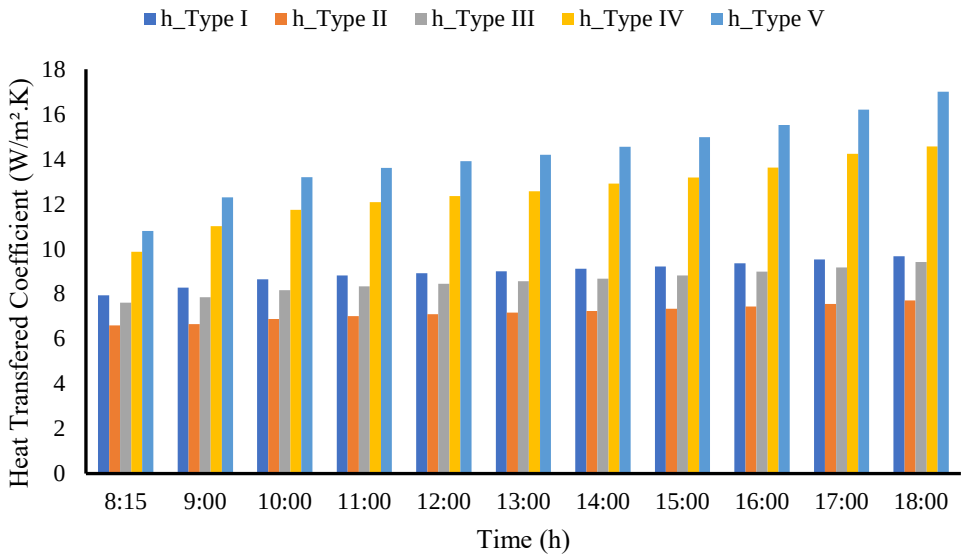

Figure 9. Heat transfer coefficients with various locations of absorber plates

Nusselt number distributions strongly depend on the absorbing plates' geometry and location. The optimal configuration allows the airflow to follow the absorbing surfaces' trajectory and contact them on both sides. There are five absorber plate locations among the absorber Types shown in Figure 10. Due to the increasing amount of area and air over the top and bottom, surface heat is removed from the heated absorber plate and transferred to the fluid.

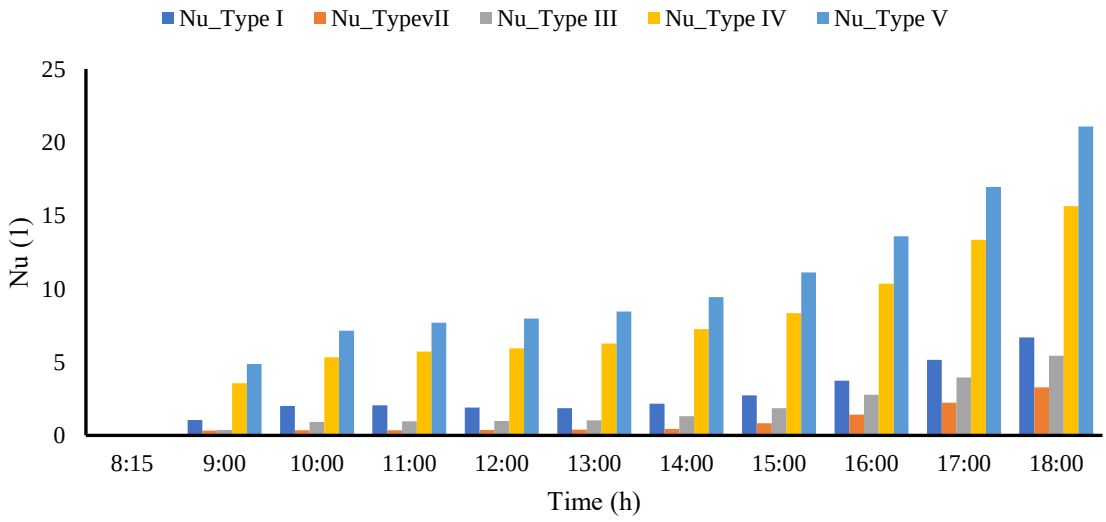

Figure 10. Nusselt Number predictions for various absorber plate locations.

In comparison to mornings and evenings, midday values decrease. Due to the higher temperature of the system's primary components at midday, there is more heat loss. The Nusselt number is greater at the end of a day than at the beginning. At a mass flow rate of 0.02 kg/s, the instantaneous Nusselt number of Type I, Type II, Type III, Type IV, and type V of SAH are compared. There are maximum values of 6.7, 3.3, 5.44, 15.64, and 21.1 for solar radiation, based on measurements.

Affect the system's thermal efficiency and air outlet temperature. This is shown in Figure 11. The temperatures at the outlet should determine the type of inlet air flow rate to use. When air is introduced at a higher rate, it reduces the system's average temperature, and as a consequence, the overall performance is improved. Due to reduced heat losses, the system achieves higher thermal efficiency. The system's thermal efficiency can be near 100% in some cases during evening hours. Therefore, this variation from the steady state represents the heat absorbed by the system components as a portion of thermal energy. At a mass flow rate of 0.02, 0.04, 0.06, and 0.08 kg/s, the instantaneous outlet temperatures with a thermal efficiency of Type V of SAH. There are maximum values of 82, 67, 58, and 53 ºC with 84.75, 93, 96.6, and 99.1%.

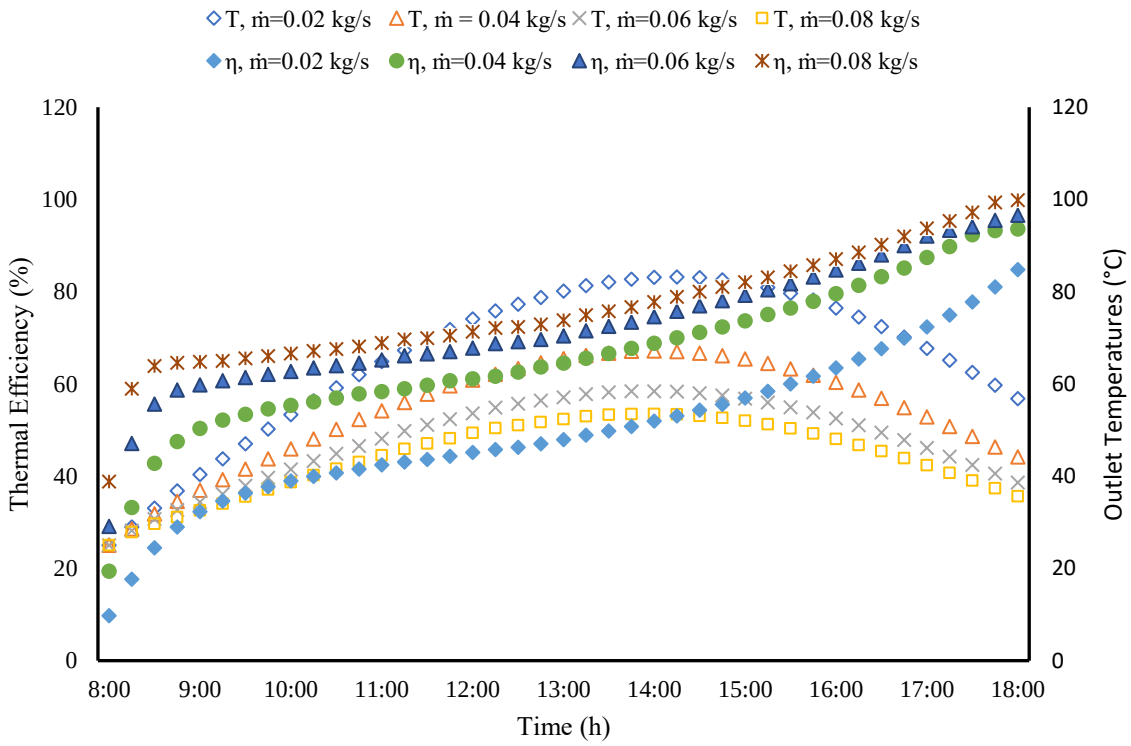

Figure 11. The air outlet temperature and thermal efficiency of the SAHs for different air inlet rates with absorber plate location Type V.

6. Conclusion

This paper investigated using an array of SAHs as a new type of solar air heater. The system's simultaneous optical and thermal analysis was conducted using coupled ray tracing and FEM simulation techniques. In the presence of non-uniform heat flux on the absorber plate surfaces, the system's thermal performance was analyzed under different operational conditions. A 3D CFD simulation was created as a model for the entire system as well as the temperature and flow rate of inlet air affected the temperature of hot air produced. There was an analysis of the thermal efficiency, heat transfer coefficient, and Nusselt number of the absorber plate at various locations in the SAHs. Due to variation in heat flux distribution, the location of the absorber plate in the collectors significantly impacts the system efficiency. To achieve the highest thermal efficiency of the system, a d of 0.012 m was determined as the most appropriate location for the absorber plate. Under specified operating conditions, Type V caused increased thermal efficiency, heat transfer coefficient, and Nusselt number compared with other types of flat plate locations.

Declaration of Competing Interest: The authors declare that they have no known competing interest

Reference

[1] Arunkumar HS, Vasudeva Karanth K, Kumar S. Review on the design modifications of a solar air heater for improvement in the thermal performance. Sustainable Energy Technologies and Assessments 2020;39.

[2] Korpale VS, Deshmukh SP, Mathpati CS, Dalvi VH. Numerical simulations and optimization of solar air heaters. Appl Therm Eng 2020;180.

[3] Khatri R, Goswami S, Anas M, Sharma S, Agarwal S, Aggarwal S. Performance evaluation of an arched plate solar air heater with porous aluminum wire mesh cylindrical fins. Energy Reports 2020;6.

[4] Zhu T, Zhang J. A numerical study on performance optimization of a micro-heat pipe arrays-based solar air heater. Energy 2021;215.

[5] Singh Bisht V, Kumar Patil A, Gupta A. Review and performance evaluation of roughened solar air heaters. Renewable and Sustainable Energy Reviews 2018;81.

[6] Singh I, Singh S. A review of artificial roughness geometries employed in solar air heaters. Renewable and Sustainable Energy Reviews 2018;92.

[7] Gilago MC, Chandramohan VP. Performance evaluation of natural and forced convection indirect type solar dryers during drying ivy gourd: An experimental study. Renew Energy 2022;182:934–45.

[8] Lingayat AB, Chandramohan VP, Raju VRK, Meda V. A review on indirect type solar dryers for agricultural crops – Dryer setup, its performance, energy storage and important highlights. Appl Energy 2020;258.

[9] Goud M, Reddy MVV, V.P. C, S. S. A novel indirect solar dryer with inlet fans powered by solar PV panels: Drying kinetics of Capsicum Annum and Abelmoschus esculentus with dryer performance. Solar Energy 2019;194:871–85.

[10] Fudholi A, Sopian K, Ruslan MH, Alghoul MA, Sulaiman MY. Review of solar dryers for agricultural and marine products. Renewable and Sustainable Energy Reviews 2010;14:1–30.

[11] Madhlopa A, Jones SA, Kalenga Saka JD. A solar air heater with composite-absorber systems for food dehydration. Renew Energy 2002;27.

[12] Sulaiman SA, Taha FFF. Drying of Oil Palm Fronds Using Concentrated Solar Thermal Power. Applied Mechanics and Materials 2014;699.

[13] Boukelia TE, Mecibah MS. Parabolic trough solar thermal power plant: Potential, and projects development in Algeria. Renewable and Sustainable Energy Reviews 2013;21:288–97.

[14] Soria R, Lucena AFP, Tomaschek J, Fichter T, Haasz T, Szklo A, et al. Modelling concentrated solar power (CSP) in the Brazilian energy system: A soft-linked model coupling approach. Energy 2016;116.

[15] Ceylan I, Gürel AE, Ergün A, Tabak A. Performance analysis of a concentrated photovoltaic and thermal system. Solar Energy 2016;129.

[16] Kasaeian A, Sharifi S, Yan WM. Novel achievements in the development of solar ponds: A review. Solar Energy 2018;174:189–206.

[17] Tabor H. Solar ponds. Solar Energy 1981;27:181–94.

[18] Madadi Avargani V, Divband M. Performance evaluation of a solar water heating system with glass-covered parabolic trough concentrators, under different system tracking modes. J Therm Anal Calorim 2022;147:4873–88.

[19] Kannan N, Vakeesan D. Solar energy for future world: - A review. Renewable and Sustainable Energy Reviews 2016;62:1092–105.

[20] Ravi Kumar K, Krishna Chaitanya NVV, Sendhil Kumar N. Solar thermal energy technologies and its applications for process heating and power generation – A review. J Clean Prod 2021;282:125296.

[21] Trefilov VI, Schur D v., Pishuk VK, Zaginaichenko SY, Choba A v., Nagornaya NR. The solar furnaces for scientific and technological investigation. Renew Energy 1999;16:757–60.

[22] Madadi Avargani V, Norton B, Rahimi A, Karimi H. Integrating paraffin phase change material in the storage tank of a solar water heater to maintain a consistent hot water output temperature. Sustainable Energy Technologies and Assessments 2021;47:101350.

[23] Gürel AE, Yıldız G, Ergün A, Ceylan İ. Exergetic, economic and environmental analysis of temperature controlled solar air heater system. Clean Eng Technol 2022;6.

[24] Jain SK, Agrawal G das, Misra R. Heat transfer augmentation using multiple gaps in arc-shaped ribs roughened solar air heater: an experimental study. Energy Sources, Part A: Recovery, Utilization and Environmental Effects 2021;43.

[25] kumar R, Kumar R, Kumar S, Thapa S, Sethi M, Fekete G, et al. Impact of artificial roughness variation on heat transfer and friction characteristics of solar air heating system. Alexandria Engineering Journal 2022;61.

[26] Sajawal M, Rehman TU, Ali HM, Sajjad U, Raza A, Bhatti MS. Experimental thermal performance analysis of finned tube-phase change material based double pass solar air heater. Case Studies in Thermal Engineering 2019;15.

[27] Abdullah AS, Amro MI, Younes MM, Omara ZM, Kabeel AE, Essa FA. Experimental investigation of single pass solar air heater with reflectors and turbulators. Alexandria Engineering Journal 2020;59.

[28] Singh AK, Agarwal N, Saxena A. Effect of extended geometry filled with and without phase change material on the thermal performance of solar air heater. J Energy Storage 2021;39:102627.

[29] Kumar A, Layek A. Evaluation of the performance analysis of an improved solar air heater with Winglet shaped ribs. Experimental Heat Transfer 2022;35.

[30] Aboghrara AM, Baharudin BTHT, Alghoul MA, Adam NM, Hairuddin AA, Hasan HA. Performance analysis of solar air heater with jet impingement on corrugated absorber plate. Case Studies in Thermal Engineering 2017;10:111–20.

[31] Luan NT, Phu NM. Thermohydraulic correlations and exergy analysis of a solar air heater duct with inclined baffles. Case Studies in Thermal Engineering 2020;21.

[32] Singh AK, Agarwal N, Saxena A. Effect of extended geometry filled with and without phase change material on the thermal performance of solar air heater. J Energy Storage 2021;39.

[33] Azad R, Bhuvad S, Lanjewar A. Study of solar air heater with discrete arc ribs geometry: Experimental and numerical approach. International Journal of Thermal Sciences 2021;167.

[34] Saravanan A, Murugan M, Reddy MS, Ranjit PS, Elumalai P v., Kumar P, et al. Thermo-hydraulic performance of a solar air heater with staggered C-shape finned absorber plate. International Journal of Thermal Sciences 2021;168.

[35] Khanlari A, Sözen A, Şirin C, Tuncer AD, Gungor A. Performance enhancement of a greenhouse dryer: Analysis of a cost-effective alternative solar air heater. J Clean Prod 2020;251.

[36] Abo-Elfadl S, Yousef MS, Hassan H. Energy, exergy, and enviroeconomic assessment of double and single pass solar air heaters having a new design absorber. Process Safety and Environmental Protection 2021;149.

[37] Singh S. Experimental and numerical investigations of a single and double pass porous serpentine wavy wiremesh packed bed solar air heater. Renew Energy 2020;145.

[38] Bensaci CE, Moummi A, Sanchez de la Flor FJ, Rodriguez Jara EA, Rincon-Casado A, Ruiz-Pardo A. Numerical and experimental study of the heat transfer and hydraulic performance of solar air heaters with different baffle positions. Renew Energy 2020;155.

[39] Yadav S, Kaushal M, Varun, Siddhartha. Nusselt number and friction factor correlations for solar air heater duct having protrusions as roughness elements on absorber plate. Exp Therm Fluid Sci 2013;44:34–41.

[40] Saini SK, Saini RP. Development of correlations for Nusselt number and friction factor for solar air heater with roughened duct having arc-shaped wire as artificial roughness. Solar Energy 2008;82:1118–30.

[41] Farhan AA, Issam M.Ali A, Ahmed HE. Energetic and exergetic efficiency analysis of a v-corrugated solar air heater integrated with twisted tape inserts. Renew Energy 2021;169.

[42] Esen H, Ozgen F, Esen M, Sengur A. Artificial neural network and wavelet neural network approaches for modelling of a solar air heater. Expert Syst Appl 2009;36:11240–8.

[43] Madadi Avargani V, Zendehboudi S, Rahimi A, Soltani S. Comprehensive energy, exergy, enviro-exergy, and thermo-hydraulic performance assessment of a flat plate solar air heater with different obstacles. Appl Therm Eng 2022;203:117907.